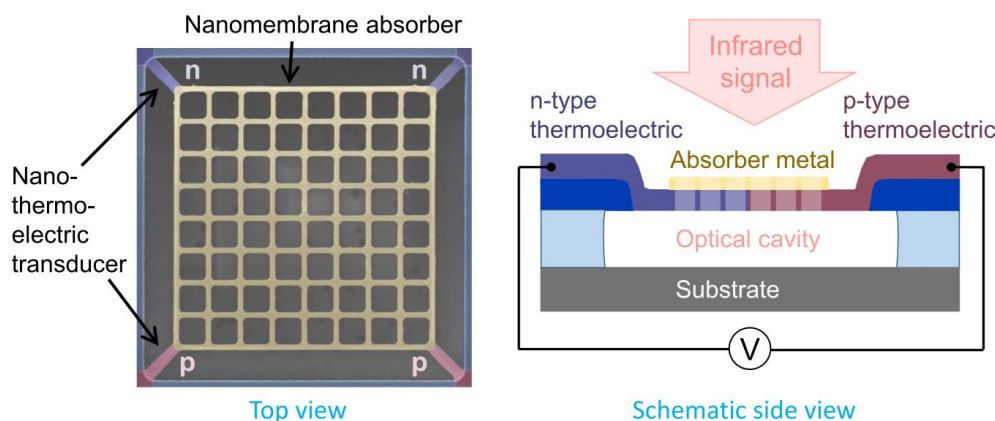


Nano-Thermoelectric Infrared Bolometer

Aapo Varpula*, Kirsi Tappura, Jonna Tiira, Kestutis Grigoras, Jouni Ahopelto, and Mika Prunnila†

VTT Technical Research Centre of Finland Ltd, Tietotie 3, FI-02150 Espoo, Finland



Abstract

Infrared (IR) radiation detectors are used in numerous applications from thermal imaging to spectroscopic gas sensing and in various fields ranging from medicine to consumer products. Thermal radiation detectors, or bolometers, which transform the radiation induced temperature rise of an absorber to electrical signal, provide a cost effective route for IR radiation detection. By combining nano-thermoelectrics and nanomembrane photonics, we demonstrate a $30 \times 30 \mu\text{m}^2$ uncooled long-wavelength IR (LWIR) bolometer that is compatible with CMOS fabrication and exhibits a very small thermal time constant of $67 \mu\text{s}$. The $24.5 \times 24.5 \mu\text{m}^2$ absorber is a 30-nm-thick metallic grid with low heat capacity, matched to vacuum impedance to guarantee high efficiency. The absorber is placed in an on-chip cavity optimized for the radiation in the spectral region around $10 \mu\text{m}$. The metal grid is supported solely by the 80 nm thick nano-thermoelectric poly-crystalline silicon beams, which convert the absorbed radiation into voltage. These transducer-support elements benefit from reduced phonon thermal conductivity, especially, due to enhanced surface scattering. The measured responsivity of the detector to LWIR radiation is 114 V/W , resulting in a specific detectivity of $1 \cdot 10^7 \text{ cmHz}^{1/2}/\text{W}$ and $4 \cdot 10^7 \text{ cmHz}^{1/2}/\text{W}$ for contact and thermoelectric beam resistance limited cases, respectively. We also show how the sensitivity of nano-thermoelectric bolometers can be improved to reach specific detectivity levels above $1 \cdot 10^9 \text{ cmHz}^{1/2}/\text{W}$ without compromising the speed of the detector. To benchmark the performance of nano-thermoelectric bolometers we briefly review the state-of-the art LWIR detectors.

1 Introduction

Infrared (IR) part of the electromagnetic spectrum, where the photon wavelength is longer than that of visible light, is relevant for numerous applications ranging from thermal imaging for night vision to remote temperature measurements and chemical analysis using infrared spectroscopy [1–3]. IR imaging and spectroscopy can be utilized for example in the detection of cancerous cells [4], thermography in medicine,

* aapo.varpula@vtt.fi

† mika.prunnila@vtt.fi

biology, and sports [5, 6] as well as in industrial applications such as bioprocess monitoring [7], and in dynamic material studies [8]. The thermal emission of most objects in the temperature range of 200–400 K is strongest in the long-wave infrared range (LWIR), typically at wavelengths 8–15 μm , thereby making this range ideal for IR applications as fully passive operation can be achieved.

In the IR range, the most common detector types are quantum detectors based on electron-hole pair generation and thermal detectors (bolometers) based on radiation-induced heating of an absorber. Quantum IR detectors, either photovoltaic or photoconductive, typically have higher sensitivity than bolometers, but require cooling from room temperature down to cryogenic temperatures to reach the maximum performance. The quantum detectors for the LWIR range require also relatively expensive and toxic materials, such as HgCdTe and InAsSb. As quantum detectors transduce the IR signal directly into electric, they are typically faster than the state-of-art thermal detectors. A high-speed detector not only provides fast data acquisition, but also enables imaging and sensing of fast processes and environments, which is a necessity, for example, in vehicular applications.

The state-of-the-art bolometers can reach relatively high sensitivities without cooling. The bolometers are essentially thermometers, which detect the temperature change of the absorber. Widely used resistive bolometers [1, 9, 10] are based on temperature-dependent resistors. Diode and transistor based bolometers [11– 13] are similar to resistive bolometers, but they use semiconductor devices as sensitive thermometers. In thermoelectric bolometers [1, 9, 10], often also referred to as thermopiles or thermocouples, the thermoelectric transduction of thermal signal into electrical signal has, in principle, low noise, as the main noise sources are the fundamental thermal fluctuation noise and the Johnson-Nyquist noise [9, 10, 14]. Furthermore, the thermoelectric transduction does not require any external power in signal generation, thus enabling low power operation. Although here we focus on detectors operating at room temperature, we note that interesting thermoelectric detector concepts have also been proposed for cryogenic temperatures [15, 16].

Traditional thermoelectrics relies on the bulk material properties, whereas, nano-thermoelectrics capitalizes on different combinations of nano-fabrication and synthesis techniques to engineer the electro-thermal performance, i.e., charge carrier and phonon transport [17–20]. Nano-thermoelectrics has been mainly driven by applications in thermal energy harvesting with very little attention to detectors until recently, when it was postulated that nano-thermoelectrics can provide an attractive low noise transduction method for bolometers [14, 21].

Silicon is an attractive detector material as it is widely used in semiconductor industry, cost-efficient, non-toxic, and, in general, abundantly available. Shaping silicon into membranes with thicknesses in the nano-scale causes its thermal conductance to collapse [22, 23] due to increased phonon scattering while keeping the Seebeck coefficient and electrical conductivity virtually unaltered. This increases the thermoelectric figure of merit significantly and, together with the maturity of the silicon technology, make Si-based nanostructures extremely attractive transducer materials for thermoelectric detectors. The feasibility of thermoelectric (non-optical) thermal detectors based on Si nanomembranes has been demonstrated recently [14, 21].

For efficient radiation-to-electricity conversion, bolometers require an efficient radiation absorber. To enhance the performance, it is essential that the absorber is supported solely by the thermoelectric legs to

reduce the thermal coupling to the surroundings. Various optical absorbers based on thin layers have been proposed and demonstrated for bolometers [24]. The thermal mass, or heat capacity, of the absorber together with the thermal conductance to the surroundings defines the speed of the bolometer. Therefore, for example for imaging applications, high absorption efficiency should be obtained with minimal absorber heat capacity.

In this work, we demonstrate a nano-thermoelectric infrared detector in which a high efficiency absorber with low heat capacity is supported by the thermoelectric transducer beams (see Fig. 1). The thermoelectric beams are highly doped poly-Si nanolayers. The thin film titanium-tungsten (TiW) grid acts, in addition to being the radiation absorber, as the electric contact between the n- and p-type beams forming the thermocouples. These material choices make the detector cost effective and CMOS compatible. The technology presented here is easily scalable to various sizes of matrices and single pixel detectors. For our $30 \times 30 \mu\text{m}^2$ pixel we obtain a very small thermal time constant $\tau = 67 \mu\text{s}$ and IR responsivity of 114 V/W resulting in a specific detectivity of $1 \cdot 10^7 \text{ cmHz}^{1/2}/\text{W}$ and $4 \cdot 10^7 \text{ cmHz}^{1/2}/\text{W}$ for contact and thermoelectric beam resistance limited cases, respectively. These results pave the way for scalable nano-thermoelectrics based IR detection technology.

2 Theory and modeling

2.1 Model of the thermoelectric bolometer

Thermoelectric bolometers can be described by a model based on lumped thermal RC circuit [10, 14, 21, 25]. The speed of the bolometer is characterized by the thermal time constant $\tau = C_{\text{th}}/G_{\text{th}}$, where C_{th} is the heat capacity of the absorber and G_{th} the thermal conductance from the absorber to the environment, which is also one of the determining factors of the bolometer sensitivity. G_{th} is a sum of the conductances stemming from two different heat transfer mechanisms, conduction and radiation, where the latter can be expressed as $G_{\text{R}} = 4A_{\text{abs}}\epsilon\sigma T^3$, where A_{abs} is the area of the absorber, ϵ the emissivity, σ the Stefan-Boltzmann constant, and T absolute temperature [14, 27]. The thermoelectric transducer of the bolometer transforms the temperature gradient between the absorber and the bath into voltage, and is characterized by the total Seebeck coefficient $S = dV/dT = S_{\text{p}} - S_{\text{n}}$, where S_{p} and S_{n} are the Seebeck coefficients of the n- and p-type thermoelectric elements.

The optical performance of the bolometer is determined by the wavelength-dependent optical (spectral) efficiency $\eta(\lambda)$ of the absorber. As the optical efficiencies of absorbers generally depend on the wavelength, the total optical efficiency η_{tot} of a bolometer is specific to the spectrum of the optical power. This optical efficiency can be written in terms of the absorbed optical power P_{abs} and the total optical power P incident on the absorber as $\eta_{\text{tot}} = \frac{P_{\text{abs}}}{P} = \frac{\int \eta(\lambda)P_{\lambda}(\lambda)d\lambda}{\int P_{\lambda}(\lambda)d\lambda}$, where $P_{\lambda}(\lambda)$ is the spectral incident optical power at wavelength λ .

The frequency dependence of the output voltage signal amplitude of a thermoelectric bolometer is given by (cf. [14, 25, 21])

$$V = \frac{V_{\text{ampl}}}{\sqrt{1 + \tau^2\omega^2}} \quad (1)$$

where ω is the angular frequency of the optical power and $V_{\text{ampl}} = S\eta_{\text{tot}}P/G_{\text{th}}$. The phase of the output voltage is

$$\theta = \arctan(-\tau\omega). \quad (2)$$

Below the thermal cut-off angular frequency of $\omega_c = 1/\tau$, eq. (1) gives $dV/dP = S\eta_{\text{tot}}/(G_{\text{th}}\sqrt{1 + \tau^2\omega^2})$, and furthermore the (voltage) responsivity of the bolometer as

$$R_V = \left. \frac{dV}{dP} \right|_{\omega \ll \omega_c} = \frac{S\eta_{\text{tot}}}{G_{\text{th}}}. \quad (3)$$

The sensitivity of a bolometer (or any photodetector) is often described by specific detectivity D^* which relates to the optical noise-equivalent power (NEP) by $D^* = \sqrt{A_{\text{abs}}}/\text{NEP}$, where NEP is defined for a unit bandwidth of 1 Hz. In thermoelectric bolometers, the main intrinsic noise sources are the Johnson-Nyquist noise associated with the total electrical resistance R of the thermoelectric transducer of the bolometer, and the thermal fluctuation noise. The latter originates from random energy exchange between the absorber of the bolometer and its surroundings by different heat carriers (electrons, phonons and photons). The corresponding optical NEP of the thermal fluctuation noise is [9]

$$\text{NEP}_{\text{th}} = \frac{\sqrt{4k_B T^2 G_{\text{th}}}}{\eta_{\text{tot}}}. \quad (4)$$

where k_B is Boltzmann's constant. For the Johnson-Nyquist noise this is given by the ratio of the Johnson-Nyquist voltage noise $v_{\text{JN}} = \sqrt{4k_B TR}$ and the frequency-dependent bolometer responsivity as $\text{NEP}_{\text{JN}}(\omega) = (dP/dV)\sqrt{4k_B TR} = R_V^{-1}\sqrt{4k_B TR}\sqrt{1 + \tau^2\omega^2}$. Below the thermal cut-off ($\omega \ll \omega_c$) this reduces to

$$\text{NEP}_{\text{JN}} = \frac{\sqrt{4k_B TR}}{R_V}. \quad (5)$$

These two independent noise sources can be combined into total optical NEP as (cf. [14, 21, 25])

$$\text{NEP} = \sqrt{\text{NEP}_{\text{th}}^2 + \text{NEP}_{\text{JN}}^2} = \text{NEP}_{\text{th}} \sqrt{1 + \frac{1}{\widetilde{ZT}}}, \quad (6)$$

where $\widetilde{ZT} = S^2 T / (G_{\text{th}} R)$ is the effective thermoelectric figure of merit of the bolometer. \widetilde{ZT} coincides with the material thermoelectric figure of merit ZT when the geometries of the n- and p-thermoelectric elements and the absolute values of the material parameters are equal [14]. Here eq. (6) is defined for the frequencies below the thermal cut off. The frequency dependency of eq. (6) can be restored by performing substitution $1/\widetilde{ZT} \rightarrow (1 + \tau^2\omega^2)/\widetilde{ZT}$. Eq. (6) shows that the fundamental thermal fluctuation noise dominates when $\widetilde{ZT} > 1/3$, and the Johnson-Nyquist noise when $\widetilde{ZT} < 1/3$. NEP can be minimized by maximizing \widetilde{ZT} and η_{tot} and by minimizing G_{th} . The maximal \widetilde{ZT} can be achieved by optimizing the geometries of the thermoelectric elements as well as their material parameters, i.e., Seebeck coefficients and electric and thermal conductivities [14].

2.2 Absorber model

The absorption of infrared radiation in the present nanobolometer shown in Fig. 1 is based on an electrically conducting absorber film (TiW), which is coupled to an optical cavity with a back reflector at the bottom of the cavity. Optically the absorber, the optical cavity, and the back reflector form a well-known quarter-wave resistive absorber, also known in radio-frequency engineering as the Salisbury screen, where the sheet resistance of the absorber is matched to the vacuum impedance [27]. This kind of structure is also known as an antiresonant interference structure [24].

The optical properties of the absorber structure are calculated with full-wave electromagnetic simulations. The three-dimensional Maxwell equations are solved using the finite element method (FEM) software Comsol Multiphysics® [28] with perfectly matched layer (PML) boundary conditions. Periodic boundary conditions perpendicular to the plane of the absorber membrane are used to generate a rectangular periodic lattice of the defined unit cell geometry. The incident radiation is simulated by plane waves that propagate normal to the surface of the detector. The dispersive permittivity of the absorber metal (TiW) is derived from the Drude model [29, 30] with the value of the electrical conductivity of $7.75 \cdot 10^5$ S/m measured for the thin TiW films and assuming the carrier relaxation time to be $1 \cdot 10^{-15}$ s. Similarly, the permittivity of polysilicon was obtained based on the Drude model, but here the doping concentration and mobility were used as the input parameters [31]. The doping concentration of the silicon substrate was $1 \cdot 10^{16}$ cm⁻³. The time-average spectral power density, Q_{abs} , absorbed in volume V is used to calculate the power absorbed in the absorber membrane [32]:

$$Q_{abs}(\omega) = \frac{\omega}{2} \int_V \text{Im}[\varepsilon(\omega)] |\mathbf{E}|^2 dV, \quad (7)$$

where E is the electric field vector and $\varepsilon(\omega)$ the dispersive permittivity, given by the Drude model, of the material in volume V .

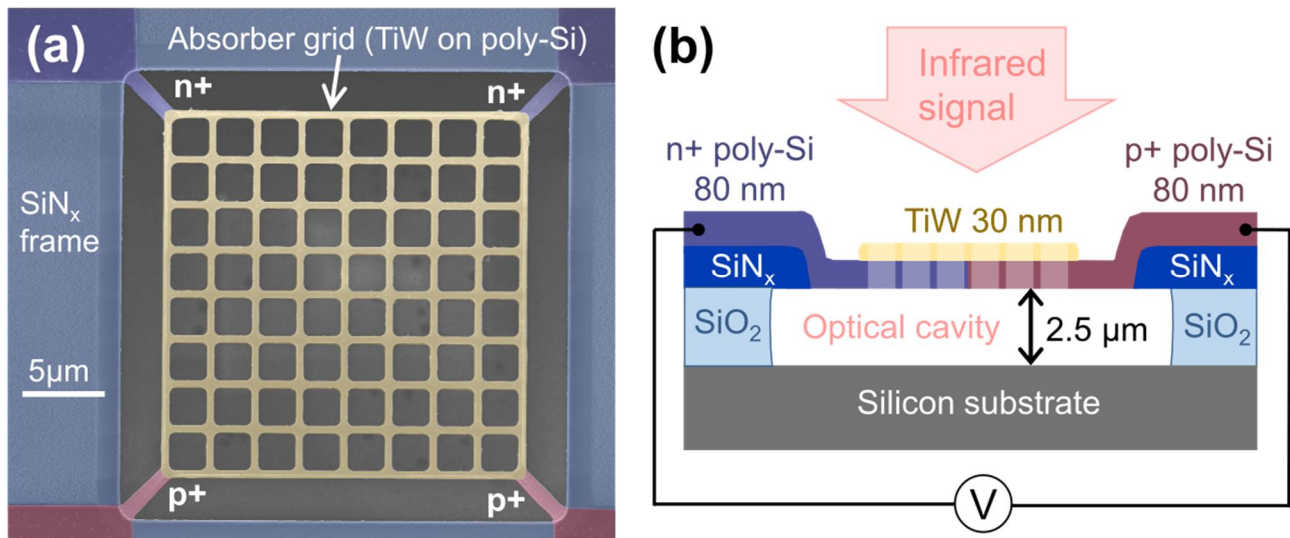


Figure 1. (a) A colored scanning electron micrograph of the nano-thermoelectric bolometer, and (b) a schematic diagonal cross-section of the device (not in scale). The absorber grid in the middle of the device consists of a stack of n- and p-doped 80 nm thick polycrystalline silicon and 30 nm thick TiW absorber metal on top. The poly-Si layer extends outside the absorber grid where it is patterned into n- and p-doped beams connected to a 270 nm thick silicon nitride frame suspended over the 2.5 μm deep optical cavity. The device consists of two n- and p-type poly-Si thermocouples connected in parallel by the TiW absorber metal.

3 Experimental

3.1 Device structure and fabrication

A scanning electron microscope image of the fabricated nano-thermoelectric bolometer is shown in Figure 1 together with a diagonal cross-section shown schematically. The device consists of an optical absorber supported by n- and p-doped 80 nm thick poly-Si beams forming two thermocouples and a silicon nitride frame controlling the strain in the beams [33]. The thermocouple pairs are electrically connected by a 30 nm thick layer of TiW, which at the same time acts as the absorbing element. This TiW-poly-Si stack absorber is patterned into a grid to control the optical impedance of the absorber, and for easier release of the suspended parts of the device during fabrication. Under the absorber grid an optical cavity is formed between the absorber and the substrate which acts as the back reflector. The optical cavity depth of 2.5 μm was selected to maximize the detector output for room-temperature thermal radiation with wavelength maximum at 10 μm .

The devices were fabricated in the VTT Micronova cleanroom facilities on a 150 mm standard single-side-polished p-type (1-50 Ωcm) silicon wafer. First, a 2.5 μm thick layer of sacrificial SiO_2 was deposited by a tetraethyl orthosilicate (TEOS) low pressure chemical vapor deposition (LPCVD) process. Next, a 270-nm-thick stress-compensation SiN_x layer was deposited by LPCVD. This SiN_x layer was patterned by plasma etching to form a strain-compensation frame similarly as in our previous work [14, 21, 33]. Then, 80 nm of LPCVD polysilicon, was deposited. The poly-Si layer was doped selectively with boron and phosphorus by ion implantation and patterned by plasma etching to form the thermoelectric beams. Resistivities of 5.3 $\text{m}\Omega\text{cm}$ and 3.4 $\text{m}\Omega\text{cm}$, charge-carrier mobilities of 27 cm^2/Vs and 15 cm^2/Vs , and Hall carrier concentrations of $4.4 \cdot 10^{19} \text{ cm}^{-3}$ and $1.3 \cdot 10^{20} \text{ cm}^{-3}$ were obtained for the n- and p-type poly-Si, respectively, using van der Pauw structures. The results are in line with the data in the literature for poly-Si films [34, 35]. After the poly-Si processing, the absorber and contact metal, 30 nm of TiW, and 300 nm Al pad metal, were sputtered and patterned by plasma and wet etching steps. Finally, the devices were released by a combination of HF vapor and HF wet etching of the sacrificial oxide layer.

3.2 Characterization

The optical characterization of the fabricated detector was performed in a vacuum chamber with pressure $< 1 \text{ Pa}$ by illuminating the sample using a calibrated cavity blackbody infrared source (model SR-200 33 of CI-Systems, emissivity 0.99 ± 0.01 , temperature accuracy $\pm 2 \text{ K}$) through a ZnSe window of the vacuum chamber lid. The detector was kept at room temperature with a temperature controlled sample holder. The total optical power is controlled by the area of the circular output aperture and the temperature of the blackbody source. To ensure that the measured signal is not caused by photovoltaic effects in silicon, a high-resistivity ($>5 \text{ k}\Omega\text{cm}$) double-side-polished silicon wafer was used as an optical filter directly in front of the ZnSe window. As Si is transparent above the wavelength of $\sim 1.1 \mu\text{m}$, the Si filter has only a minor effect on the shape of the mid and long-wave infrared spectrum used in the experiments. The combination of the ZnSe window and the high resistivity Si filter results in a relatively flat transmission in the wavelength range of 1–20 μm . The total IR power incident on the detector absorber through the optical system is estimated using a numerically calculated blackbody spectrum and the analytical model of the optical setup with a Lambertian blackbody source (cf. [36]).

The opto-thermoelectric response of the detector was measured with a lock-in technique using an optical chopper, a SR865A lock-in amplifier and a SR560 preamplifier connected to the detector in a differential mode. In the measurement, the two thermocouples of the bolometer were connected in parallel, i.e., the n+ ends of the two thermocouples were connected together as well as the p+ ends (see Fig. 1). In high-frequency response measurements an optical chopper wheel with smaller slits, and thus, a small output aperture for the infrared radiation is needed. Therefore, the optical power was maximized by using a high blackbody temperature.

4 Results and discussion

The measured frequency response of the IR detector of Fig. 1 is shown in Fig. 2. The first order response model of eqs. (1) and (2) fits well both to the experimental amplitude and phase data. We can observe that our thermal detector is extremely fast: The model fit yields the detector thermal time constant of $66.7 \mu\text{s}$, which is exceptionally small for a thermal detector. The corresponding thermal cut-off frequency $\omega_c/2\pi$ is 15 kHz suggesting that the detector is capable of detecting optical signals with frequencies up to tens of kHz depending of the power of the measured signal.

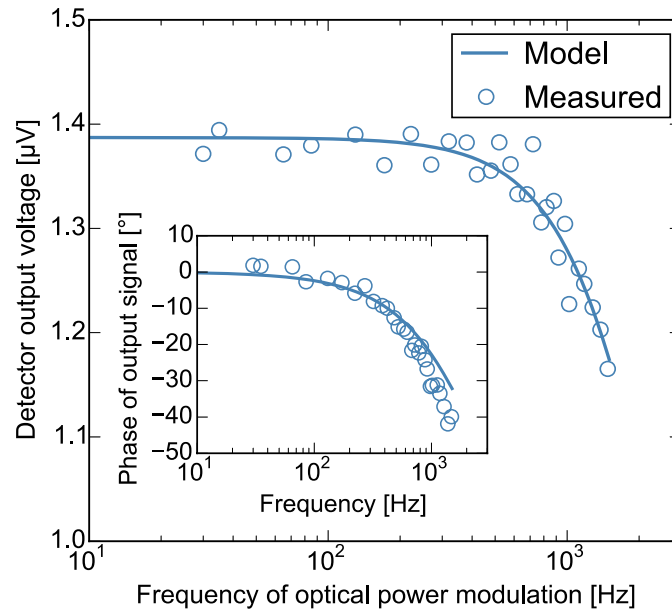


Figure 2. Frequency response of the infrared detector. The response model of eq. (1) was fitted to the measured detector output voltage amplitude as a function of the frequency of the optical power modulation. The fitting parameters are $\tau = 66.7 \pm 2.4 \mu\text{s}$ and $V_{\text{ampl}} = 1387 \pm 5 \text{ nV}$. The inset shows the measured phase of the detector output signal as well as the fitted model response of eq. (2). The temperature of the blackbody infrared source is $1200 \text{ }^\circ\text{C}$, and the total optical power incident on the absorber area is $20 \pm 8 \text{ nW}$.

Fig. 3a shows the response of the detector to blackbody infrared signals with power levels extending two orders of magnitude. They were measured at low frequencies below the thermal cutoff. The response data shows good linearity over the whole power range, thereby demonstrating excellent dynamic range of the detector. The spectral efficiency of the absorber $\eta(\lambda)$, simulated using circularly polarized IR radiation, is shown in Fig. 3b. The response of the absorber is independent of the polarization. In Fig. 3b the spectral efficiency of the absorber $\eta(\lambda)$ peaks around the wavelength of $10 \mu\text{m}$, thus making the present bolometer ideal for thermal signals from bodies around room temperature. The peak of the blackbody radiation shifts to lower wavelengths at higher blackbody temperatures (e.g. $6.1 \mu\text{m}$ $200 \text{ }^\circ\text{C}$ and $2.7 \mu\text{m}$ at $800 \text{ }^\circ\text{C}$), which

results in a slight reduction of the responsivity of the detector. However, the intensity of the blackbody radiation increases at all wavelengths and, thereby, the total detected signal grows as a function of the temperature of the blackbody regardless of the optimal wavelength range of the detector.

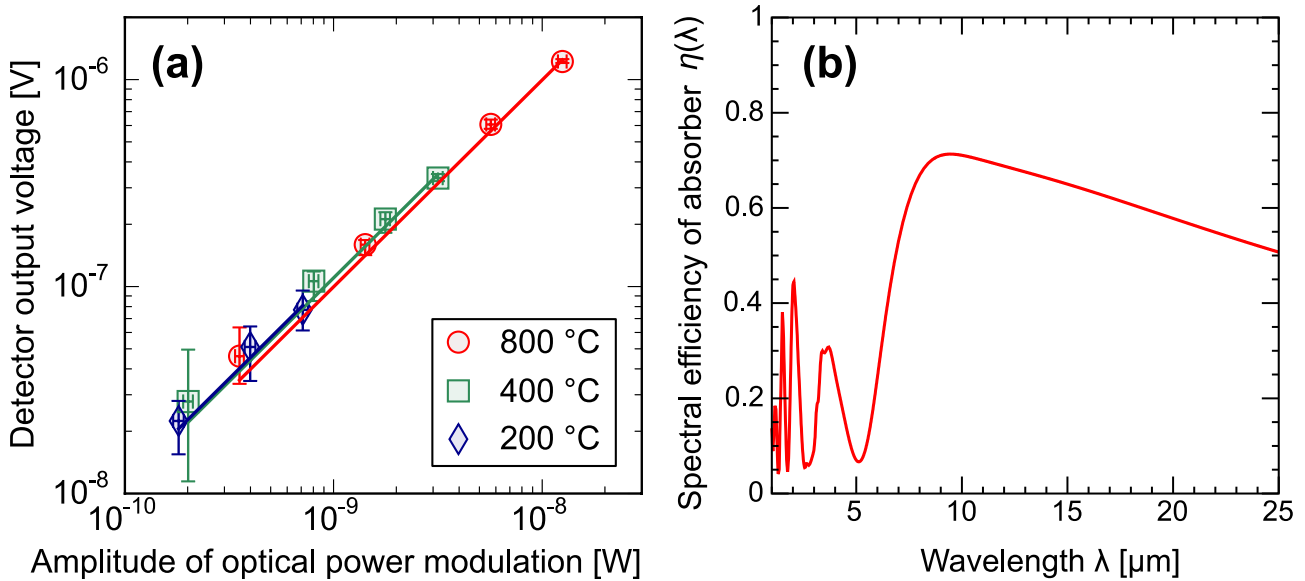


Figure 3. (a) The power response of the detector measured using various temperatures and output apertures of the blackbody infrared source. The power amplitude is the total optical power incident on the absorber area. The linear fits to the data (solid lines) correspond to the responsivities of 113.6 ± 6 V/W (200 °C), 110.1 ± 5 V/W (400 °C), and 99.5 ± 3 V/W (800 °C). (b) Simulated spectral efficiency of the absorber $\eta_{\text{abs}}(\lambda)$ as a function of the optical signal wavelength. The spectral efficiency does not reach unity due to the use of suboptimal back reflector and slight mismatch of optical impedance (see text for details).

The FEM simulations of the poly-Si-TiW absorber grid showed that the TiW layer governs the optical absorption process in the bolometer, and the poly-Si layer below the TiW layer is mostly inactive because its electric conductivity is too low at IR frequencies. The optical impedance matching of the TiW layer is determined by the TiW sheet resistance resulting in impedance of 287 Ω instead of the optimal 377 Ω . However, the effect of this mismatch is small: We estimate a reduction of the peak absorptance from 100% to 98 – 99% when an ideal back reflector is utilized with the present absorber. The optimal impedance matching can be achieved by tuning the geometry of the absorber grid or the thickness of the TiW layer. Another way to improve the absorptance is to increase the reflectance of the back reflector from the Si substrate value of 30%, for example by introducing a metal layer on top of the substrate. These straightforward improvements would allow the absorptivity to be increased virtually to 100%.

Eq. (3) allows the estimation of the material parameters of the thermoelectric transducer of the detector. The literature data on LPCVD polycrystalline silicon with similar resistivities as in the present work [34, 37] suggest that the Seebeck coefficients of the n- and p-type poly-Si are $-0.25 \dots -0.30$ mV/K and $0.2 - 0.25$ mV/K, respectively. Based on these values, the total Seebeck coefficient S of the detector is $0.45 - 0.55$ mV/K, which is consistent with our previous results [21]. Using the 200 °C value of $R_V = 113.6$ V/W (see Fig. 3a) and the simulated total optical efficiency of absorber $\eta_{\text{tot}} = 0.509$, eq. (3) gives $S/G_{\text{th}} = 223$ V/W. Furthermore, with the estimated S , we obtain $2.0 - 2.5$ $\mu\text{W}/\text{K}$ for the thermal conductance G_{th} of the detector. By assuming that thermal conductivities of the n- and p-type poly-Si beams are equal, this corresponds to thermal conductivities of $26 - 32$ W/m/K. These values are in line with the thermal conductivities of undoped and

doped single and polycrystalline silicon membranes with similar thickness ranges [14, 21–23, 35]. Thicker poly-Si films with higher doping levels than in the present poly-Si membranes and bulk poly-Si exhibit thermal conductivities in the range 30 – 120 W/m/K [37–39]. The thermal conductivity of the present poly-Si membranes suggests that phonon surface scattering reduces the thermal conductivity similarly as in single-crystalline Si nanomembranes [22, 23].

The total resistance R of the thermoelectric transducer has a dominant effect on the sensitivity of the device as it determines the intrinsic voltage noise of the detector [14]. The characteristics of the present bolometer are summarized in Table 1. It is important to notice that while the total resistance of the thermoelectric transducer is 50 k Ω , only a small portion of it, namely $R_{\text{beams}} = 2.8$ k Ω , arises from the thermoelectric poly-Si beams. Ideally, the resistance of the absorber grid has only little contribution to the total resistance of the device as the effective sheet resistance of the absorber grid is equal to the vacuum impedance (~ 377 Ω). The extra resistance arises from the resistance of the polysilicon–TiW contact in the absorber grid requiring further process and material optimization. The values of R listed in Table 1 and the value of G_{th} estimated above give $\widetilde{ZT} = 6\text{--}7 \cdot 10^{-4}$ using the measured total bolometer resistance, and $\widetilde{ZT} = 0.011\text{--}0.013$ using the resistance of the thermoelectric beams only.

Table 1. Summary of characteristics of the nano-thermoelectric IR bolometer.

Total device area A [μm^2]	30 x 30
Absorber area A_{abs} [μm^2]	24.5 x 24.5
Absorber fill factor $\eta_{\text{FF}} = A_{\text{abs}}/A$	66.7%
Measured thermal time constant τ [μs]	66.7 ± 2.4
Total bolometer resistance [k Ω]	50
Resistance of thermoelectric beams R_{beams} [k Ω]	2.8
Measured responsivity ^a R_V [V/W]	113.6 ± 6
Optical noise equivalent power ^a (NEP) [pW/Hz ^{1/2}]	$252 \pm 13^{\text{b}} / 59.6^{\text{c}}$
Specific detectivity ^a D^* [10^6 cmHz ^{1/2} /W]	$9.73 \pm 0.5^{\text{b}} / 41.1^{\text{c}}$

^aSensitivity to 200 °C blackbody radiation.

^bSensitivity determined by total resistance, which is limited by contact resistance. Calculated using eq. (5) with $R = 50$ k Ω .

^cLimiting sensitivity determined by the resistance of the thermoelectric beams. Calculated using eq. (5) with $R = R_{\text{beams}} = 2.8$ k Ω .

Because the estimated \widetilde{ZT} is well below 1/3, the intrinsic voltage noise of the present bolometer is determined by the Johnson-Nyquist noise, see eq. (6) and Ref. [14]. This allows us to calculate the optical NEP = 252 pW/Hz^{1/2} and specific detectivity $D^* = \sqrt{A_{\text{abs}}}/\text{NEP} = 9.73 \cdot 10^6$ cmHz^{1/2}/W using eq. (5) by applying the total bolometer resistance R . In the ideal case, the thermoelectric beams alone (R_{beams}) determine the total resistance R of the bolometer, which would decrease the NEP and increase D^* from the measured values to NEP = 59.6 pW/Hz^{1/2} and $D^* = 4.11 \cdot 10^7$ cmHz^{1/2}/W. These calculated and estimated parameters are listed also in Table 1 As discussed above, the total optical efficiency η_{tot} of the bolometer can be increased to 100%

by improving the absorber efficiency. In this case $NEP = 128 \text{ pW/Hz}^{1/2}$ and $D^* = 1.91 \cdot 10^7 \text{ cmHz}^{1/2}/\text{W}$ would be reached with $R = 50 \text{ k}\Omega$ resistance, and $NEP = 30.3 \text{ pW/Hz}^{1/2}$ and $D^* = 8.09 \cdot 10^7 \text{ cmHz}^{1/2}/\text{W}$ with $2.8 \text{ k}\Omega$ resistance, respectively. This former estimate of NEP coincides also with the estimated electrical NEP of the detector. Furthermore, \widetilde{ZT} and thereby NEP and D^* of the present bolometer can be improved by selecting optimal geometries for the thermoelectric beams based on the resistivities, and Seebeck coefficients and thermal conductivities of the n- and p-type thermoelectric materials (see Ref. [14] and further discussion on \widetilde{ZT} below). These calculations show that optical NEP well below $100 \text{ pW/Hz}^{1/2}$ and D^* above $5 \cdot 10^7 \text{ cmHz}^{1/2}/\text{W}$ can be reached by reducing R and increasing η_{tot} of the present bolometer. The performance can be improved even further by geometrical optimization of \widetilde{ZT} .

4.1 Routes to optimize the performance

Since the surface scattering of phonons increase with decreasing nanomembrane thickness, leading to decrease in thermal conductivity [23], the performance of the thermoelectric transducer of the detector can be improved by thinning the poly-Si membrane. Further performance enhancement can be achieved by maximizing the power factor S^2/R by optimizing the doping parameters. However, since S decreases with increasing electric conductivity [20], the optimization is more complicated than just minimizing of R by increasing the doping. The effect of a thinner poly-Si membrane can be estimated using the experimental data from a 9 nm thick single-crystalline silicon layer with native oxide, which exhibits thermal conductivity of 8 W/m/K [23]. If it is assumed that S and the electric conductivity of the nanomembrane remain the same, then we can use the proportionalities $G_{\text{th}} \propto \kappa t$ and $\widetilde{ZT} \propto (G_{\text{th}} R)^{-1} \propto \kappa^{-1}$, where t is the thickness and κ the thermal conductivity of the n- and p-type poly-Si (assumed here to be equal for both the doping types). If the thickness could be reduced from 80 nm to 9 nm, then κ would reduce from 32 W/m/K to 8 W/m/K , and G_{th} of the present detector would reduce from $2.5 \text{ }\mu\text{W/K}$ to 70 nW/K . The contribution from the radiative heat conductance G_{R} can be neglected in these estimates as $G_{\text{R}} = 3.9 \text{ nW/K}$ (assuming $\epsilon = 1$ and $T = 300 \text{ K}$) for the present detector. The thickness reduction would increase \widetilde{ZT} from 0.013 to 0.052 (in the case R is dominated by the electric resistance of the thermoelectric beams R_{beams}). Furthermore, we assume that power factor S^2/R can be doubled leading to $\widetilde{ZT} = 0.104$. Next, we assume that $\eta(\lambda)$ can be increased to 1 at all the wavelengths of interest in the hypothetical 9 nm poly-Si device, leading to $NEP_{\text{th}} = 0.59 \text{ pW/Hz}^{1/2}$, $NEP = 1.9 \text{ pW/Hz}^{1/2}$, and $D^* = 1.3 \cdot 10^9 \text{ cmHz}^{1/2}/\text{W}$ [see eqs. (4) and (6)]. We refer this estimated case as A.

The effect of the thickness reduction of the poly-Si nanomembrane on τ can be estimated using the bulk values of the volumetric heat capacities of Si and the TiW absorber metal. We use a value of Ti for TiW, as Ti has slightly higher volumetric heat capacity than W. This rough calculation shows that the poly-Si thickness of 9 nm would reduce C_{th} by 64.6%. With the decreased G_{th} calculated above, this leads to estimated τ of $836 \text{ }\mu\text{s}$ (case A). For $D^* = 1.3 \cdot 10^9 \text{ cmHz}^{1/2}/\text{W}$ estimated above this time constant is a signature of high temporal performance for a thermal detector. Alternatively, the thermoelectric beams of the detector could be shortened so that G_{th} would remain $2.5 \text{ }\mu\text{W/K}$ and the fill factor $\eta_{\text{FF}} = A_{\text{abs}}/A$ would increase to 90%. The resulting device (case B) would be both faster and much more sensitive than the device with 80 nm poly-Si as the estimated performance values are $\tau = 23.6 \text{ }\mu\text{s}$, $NEP_{\text{th}} = 3.9 \text{ pW/Hz}^{1/2}$, $NEP = 13 \text{ pW/Hz}^{1/2}$, and $D^* = 2.3 \cdot 10^8 \text{ cmHz}^{1/2}/\text{W}$ [see eqs. (4) and (6)].

The performance of our nano-thermoelectric bolometer is compared in Fig. 4 with results reported in the literature for thermal LWIR detectors. For reference, cooled and uncooled quantum LWIR detectors are also included in Fig. 4. The present bolometer is an order of magnitude faster than the fastest state-of-the-art

thermoelectric bolometer and 3 times faster than the fastest state-of-the-art resistive bolometers. The sensitivity of the present device is in the same order of magnitude as some thermal detectors and most uncooled quantum detectors. The fill factor of the present device $\eta_{FF} = 67\%$ is large compared to the fill factors of many existing thermoelectric bolometers [56, 58], as an example the detector in Ref. [54] has a fill factor of 1%. Detectors with a large fill factor are attractive in imaging applications where tightly packed detector arrays are needed. As discussed above, we expect that the performance of the present device can be improved remarkably by straightforward material and geometrical optimization. In addition, Fig. 4 shows the performance values of the resistance-optimized nano-thermoelectric bolometer with the total resistance R determined by the beams only (see Table 1) as well as the proposed optimized detectors based on 9 nm poly-Si designed either for speed (case B) or sensitivity (case A), as described in the previous section. The detector sensitivity can be enhanced further by utilizing high ZT materials [60–63], which allow NEP to be pushed to the thermal fluctuation limit.

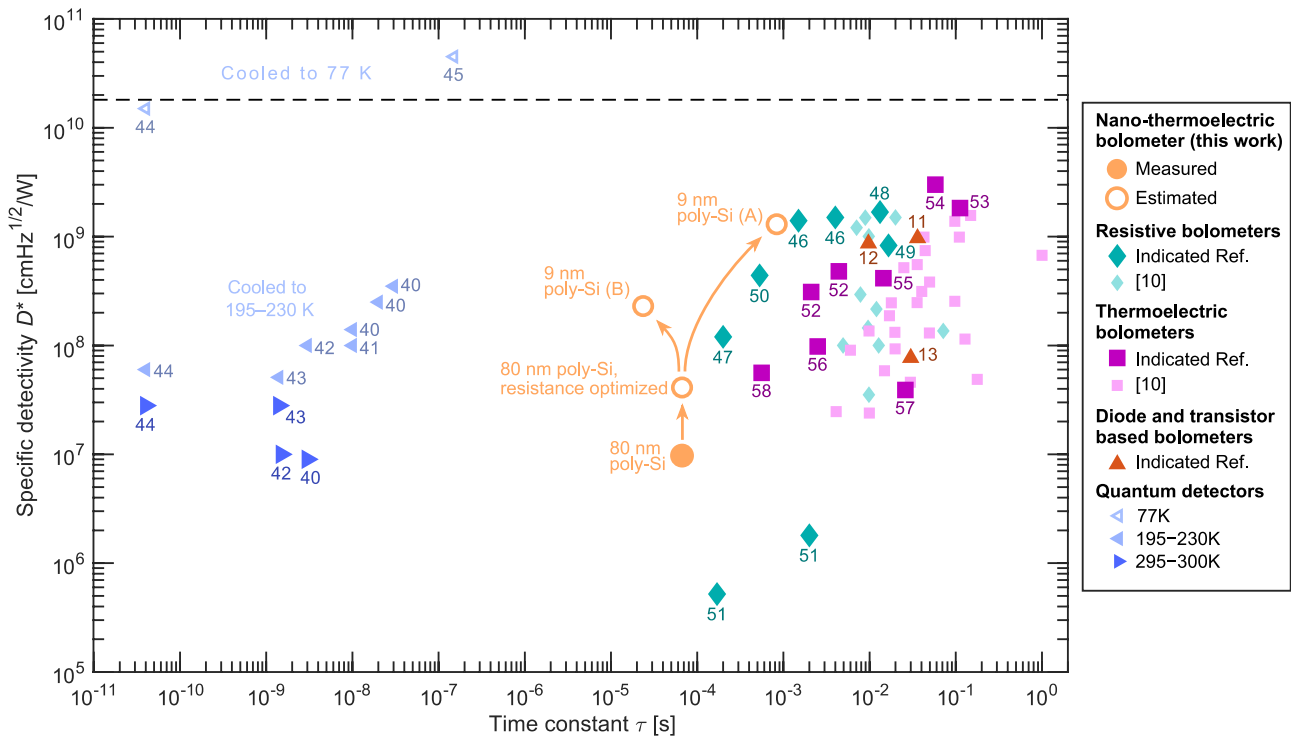


Figure 4. Time constants τ and specific detectivities D^* of the nano-thermoelectric bolometer presented in this work and of commercial and non-commercial LWIR bolometers and quantum LWIR detectors [11–13, 40–58]. The data of this work includes measured and estimated detectors based on 80 nm poly-Si, and estimated cases A and B with 9 nm poly-Si and different beam and absorber geometries. The dashed black line shows the 290 K background radiation limit for thermal detectors calculated using full spectrum in the half space case [59]. The D^* values of Refs. [57] and [13] were calculated using the reported responsivity, NEP, and geometrical data.

5 Conclusions

In conclusion, by combining nano-thermoelectrics and nanomembrane photonics, we have demonstrated a CMOS-compatible LWIR bolometer. The measured responsivity of the bolometer was 114 V/W giving a specific detectivity of $1 \cdot 10^7$ cmHz^{1/2}/W and $4 \cdot 10^7$ cmHz^{1/2}/W for contact resistance and thermoelectric beam resistance limited cases, respectively. The detector exhibited a very small thermal time constant of 67 μ s. The fast operation speed stemmed from the low heat capacity multi-functional absorber, where a single

metal layer grid absorbs the radiation and, at the same time, connects the poly-silicon n- and p-type nano-thermoelectric support beams, which convert the IR radiation induced temperature rise into voltage. We discussed how the specific detectivity of nano-thermoelectric bolometers can be pushed above $1 \cdot 10^9$ $\text{cmHz}^{1/2}/\text{W}$ without compromising the speed of the detector and benchmarked the performance with the state-of-the art LWIR detectors

Acknowledgements

This work has been financially supported by the European Union Seventh Framework Programme (Grant Agreement No. 604668, project QUANTIHEAT), by European Union Future and Emerging Technologies (FET) Open under Horizon 2020 programme (Grant Agreement No. 766853, project EFINED), by Business Finland co-innovation project RaPtor (No. 6030/31/2018) and by the Academy of Finland (Grant No. 295329 and 314447). The work of Jonna Tiira was supported by Academy of Finland (Grant No. 324838). We acknowledge gratefully the technical assistance of Teija Häkkinen, Kai Viherkanto, Paula Holmlund, Tahvo Havia and Olli-Pekka Kilpi in device fabrication and characterization.

References

- [1] H. Budzier and G. Gerlach, "Thermal infrared sensors: theory, optimisation and practice", Wiley (2011).
- [2] F. Baldini et al., "Optical Chemical Sensors", Springer (2006).
- [3] Daniel Popa and Florin Udrea, "Towards Integrated Mid-Infrared Gas Sensors", *Sensors* 19, 2076 (2019).
- [4] Giuseppe Bellisola and Claudio Sorio, "Infrared spectroscopy and microscopy in cancer research and diagnosis", *American Journal of Cancer Research* 2 (1), 1–21 (2012).
- [5] Glenn J. Tattersall, "Infrared thermography: A non-invasive window into thermal physiology", *Comparative Biochemistry and Physiology, Part A* 202, 78–98 (2016).
- [6] Jose Ignacio Priego-Quesada, *Application of Infrared Thermography in Sports Science*, Springer International Publishing, 2017.
- [7] Daniel Landgrebe, Claas Haake, Tim Höpfner, Sascha Beutel, Bernd Hitzmann, Thomas Scheper, Martin Rhiel, and Kenneth F. Reardon, "On-line infrared spectroscopy for bioprocess monitoring", *Applied Microbiology and Biotechnology* 88 (1), 11–22 (2010).
- [8] Ming-Wei Chen, Sizhu You, Kenneth S. Suslick, and Dana D. Dlott, "Hot spots in energetic materials generated by infrared and ultrasound, detected by thermal imaging microscopy", *Review of Scientific Instruments* 85, 023705 (2014).
- [9] P. L. Richards, "Bolometers for infrared and millimeter waves", *Journal of Applied Physics* 76, 1 (1994).

- [10] U. Dillner, E. Kessler, H.-G. Meyer, "Figures of merit of thermoelectric and bolometric thermal radiation sensors", *J. Sens. Sens. Syst.* 2, 85 (2013).
- [11] Selim Eminoglu, Mahmud Yusuf Tanrikulu, and Tayfun Akin, "A Low-Cost 128 × 128 Uncooled Infrared Detector Array in CMOS Process", *Journal of Microelectromechanical Systems* 17 (1), 20–30 (2008).
- [12] Liang Dong, Ruifeng Yue, and Litian Liu, "Fabrication and Characterization of Integrated Uncooled Infrared Sensor Arrays Using a-Si Thin-Film Transistors as Active Elements", *J. Microelectromech. Syst.* 14 (5), 1167–1177 (2005).
- [13] L. Gitelman, S. Stolyarova, S. Bar-Lev, Z. Gutman, Y. Ochana, and Y. Nemirovsky, "CMOS-SOI-MEMS Transistor for Uncooled IR Imaging", *IEEE Trans. Elec. Dev.* 56 (9), 1935–1942 (2009).
- [14] A. Varpula, A. V. Timofeev, A. Shchepetov, K. Grigoras, J. Hassel, J. Ahopelto, M. Ylilammi, and M. Prunnila, "Thermoelectric thermal detectors based on ultra-thin heavily doped single-crystal silicon membranes", *Applied Physics Letters* 110, 262101 (2017).
- [15] T. T. Heikkilä, R. Ojajärvi, I. J. Maasilta, E. Strambini, F. Giazotto, and F. S. Bergeret, "Thermoelectric Radiation Detector Based on Superconductor-Ferromagnet Systems", *Phys. Rev. Applied* 10, 034053 (2018).
- [16] A. Gulian, K. Wood, D. van Vechten, and G. Fritz, "Cryogenic thermoelectric (QVD) detectors: Emerging technique for fast single-photon counting and non-dispersive energy characterization", *Journal of Modern Optics* 51 (9–10), 1467–1490 (2004).
- [17] Hilaal Alam and Seeram Ramakrishna, "A review on the enhancement of figure of merit from bulk to nano-thermoelectric materials", *Nano Energy* 2 (2), 190–212 (2013).
- [18] Zhi-Gang Chen, Guang Han, Lei Yang, Lina Cheng, and Jin Zou, "Nanostructured thermoelectric materials: Current research and future challenge", *Progress in Natural Science: Materials International* 22 (6), 535–549 (2012).
- [19] Weishu Liu, Jizhen Hu, Shuangmeng Zhang, Manjiao Deng, Cheng-Gong Han, and Yong Liu, "New trends, strategies and opportunities in thermoelectric materials: A perspective", *Materials Today Physics* 1, 50-60 (2017).
- [20] Ali Shakouri, "Recent Developments in Semiconductor Thermoelectric Physics and Materials", *Annual Review of Materials Research* 41, 399–431 (2011).
- [21] A. Varpula, K. Grigoras, K. Tappura, A. V. Timofeev, A. Shchepetov, J. Hassel, J. Ahopelto, and M. Prunnila, "Silicon Based Nano-Thermoelectric Bolometers for Infrared Detection", *Proceedings* 2 (13), 894, *Proceedings of EUROSENSORS 2018, Graz, Austria, 9-12 September 2018.*
- [22] E. Chávez-Ángel, J. S. Reparaz, J. Gomis-Bresco, M. R. Wagner, J. Cuffe, B. Graczykowski, A. Shchepetov, H. Jiang, M. Prunnila, J. Ahopelto, F. Alzina, and C. M. Sotomayor Torres, "Reduction of the thermal

conductivity in free-standing silicon nano-membranes investigated by non-invasive Raman thermometry", *APL Materials* 2, 012113 (2014).

[23] S. Neogi, J.S. Reparaz, L. F. C. Pereira, B. Graczykowski, M. R. Wagner, M. Sledzinska, A. Shchepetov, M. Prunnila, J. Ahopelto, C. M. Sotomayor-Torres, and D. Donadio, "Tuning Thermal Transport in Ultrathin Silicon Membranes by Surface Nanoscale Engineering", *ACS Nano* 9, 3820-3828 (2015).

[24] J. J. Talghader, A. S. Gawarikar, and R. P. Shea, "Spectral selectivity in infrared thermal detection", *Light: Science & Applications* 1, e24 (2012).

[25] A. Varpula, A. V. Timofeev, A. Shchepetov, K. Grigoras, J. Ahopelto, and M. Prunnila, "Thermoelectric bolometers based on silicon membranes", *Proceedings of SPIE* 10246, 102460L (2017).

[26] A. Rogalski, "Infrared Detectors", Gordon Breach Science Publishers, 2000.

[27] Ben A. Munk, "Frequency selective surfaces: Theory and design", John Wiley Sons Inc. New York, 2000.

[28] COMSOL Multiphysics® v. 5.3. www.comsol.com. COMSOL AB, Stockholm, Sweden.

[29] P. K. L. Drude, "Theory of Optics", Dover, New York, U.S.A., 1959.

[30] R. A. Paquin, Chapter 35: Properties of metals", in *Handbook of optics, Volume II*, Ed. Michael Bass, McGraw-Hill, Inc., New York, U.S.A., 1995.

[31] Paul M. Amirtharaj and David G. Seiler, Chapter 36: Optical properties of semiconductors, in *Handbook of optics, Volume II*, Ed. Michael Bass, McGraw-Hill, Inc., New York, U.S.A., 1995.

[32] K. Tappura, J. Luomahaara, T. Haatainen, J. Hassel, T. Vehmas, *Plasmonics* 11, 627-635 (2016).

[33] A. Shchepetov, M. Prunnila, F. Alzina, L. Schneider, J. Cuffe, H. Jiang, E. I. Kauppinen, C. M. Sotomayor Torres, and J. Ahopelto, "Ultra-thin free-standing single crystalline silicon membranes with strain control", *Applied Physics Letters* 102, 192108 (2013).

[34] Hideo Muro, Takeshi Mitamura, and Shigeyuki Kiyota, "Determination of electrical properties of n-type and p-type polycrystalline silicon thin films as sensor materials", *Sensors and Materials* 18 (8), 433-444 (2006).

[35] Durgadevi Elamaran, Hiroaki Satoh, Norihisa Hiromoto, and Hiroshi Inokawa, "Investigation of silicon-on-insulator CMOS integrated thermocouple and heater for antenna-coupled bolometer", *Japanese Journal of Applied Physics* 58, SDDE08 (2019).

[36] Edward F. Zalewski, Chapter 24: Radiometry and photometry, in *Handbook of optics, Volume II*, Ed. Michael Bass, McGraw-Hill, Inc., New York, U.S.A., 1995.

- [37] Jin Xie, Chengkuo Lee, Ming-Fang Wang, Youhe Liu and Hanhua Feng, "Characterization of heavily doped polysilicon films for CMOS-MEMS thermoelectric power generators", *J. Micromech. Microeng.* 19, 125029 (2009).
- [38] M. Strasser, R. Aigner, C. Lauterbach, T.F. Sturm, M. Franosch, G. Wachutka, "Micromachined CMOS thermoelectric generators as on-chip power supply", *Sensors and Actuators A: Physical* 114 (2–3), 362-370 (2004).
- [39] A. Stranz, J. Kähler, A. Waag, and E. Peiner, "Thermoelectric Properties of High-Doped Silicon from Room Temperature to 900 K", *Journal of Electronics Materials* 42 (7), 2381-2387 (2013).
- [40] Photoconductive MCT detector data in Catalog 2018/2019, p. 6, VIGO System S.A., <https://vigo.com.pl/wp-content/uploads/2017/06/VIGO-Catalogue.pdf>
- [41] Photovoltaic MCT detector data in Catalog 2018/2019, p. 10, VIGO System S.A., <https://vigo.com.pl/wp-content/uploads/2017/06/VIGO-Catalogue.pdf>
- [42] Photovoltaic multiple junction MCT detector data in Catalog 2018/2019, p. 14, VIGO System S.A., <https://vigo.com.pl/wp-content/uploads/2017/06/VIGO-Catalogue.pdf>
- [43] Hamamatsu, Data of photovoltaic InAsSb detector P13894-211MA from <https://www.hamamatsu.com/eu/en/product/optical-sensors/infrared-detector/inassb-photovoltaic-detector/index.html>, and https://www.hamamatsu.com/resources/pdf/ssd/p13894_series_kird1133e.pdf
- [44] Daniele Palaferri, Yanko Todorov, Azzurra Bigioli, Alireza Mottaghizadeh, Djamal Gacemi, Allegra Calabrese, Angela Vasanelli, Lianhe Li, A. Giles Davies, Edmund H. Linfield, Filippos Kapsalidis, Mattias Beck, Jérôme Faist, and Carlo Sirtori, "Room-temperature nine- μm -wavelength photodetectors and GHz-frequency heterodyne receivers", *Nature* 556, 85-88 (2018).
- [45] Teledyne, Data of photoconductive MCT detector J15D12-M204-S025U-60 from <http://www.teledynejudson.com/prods/Pages/Photoconductive-Mercury-Cadmium-Telluride-Detectors.aspx>
- [46] W. Schnelle, U. Dillner, B. Scheike, L. Albrecht, "Infrared radiation sensors based on thin film bolometers", 11th International Symposium of the Technical Committee on Photon-Detectors, Weimar, GDR, 11-13 September, 1984 / [edited by J. Schanda, K.H. Herrmann, and I. Ungvári]
- [47] Mahmoud Almasri, Donald P. Butler, and Zeynep Çelik-Butler, "Self-Supporting Uncooled Infrared Microbolometers With Low-Thermal Mass", *J. Microelectromech. Syst.* 10 (3), 469–476 (2001).
- [48] Liang Dong, Rui-Feng Yue, Li-Tian Liu, "An Uncooled Microbolometer Infrared Detector Based on Polycrystalline Silicon Germanium Thin Film", *International Journal of Nonlinear Sciences and Numerical Simulation* 3, 303–306 (2002).

- [49] Liang Dong, Ruifeng Yue, Litian Liu, "An uncooled microbolometer infrared detector based on poly-SiGe thermistor", *Sensors and Actuators A* 105, 286–292 (2003).
- [50] Shivaprasad Karanth, M.A. Sumesh, V. Shobha, H. Ganesh Shanbhogue, C.L. Nagendra, "Infrared detectors based on thin film thermistor of ternary Mn–Ni–Co–O on micro-machined thermal isolation structure", *Sensors and Actuators A: Physical* 153, 69–75 (2009).
- [51] Wei Zhou, Yiming Yin, Jing Wu, Yanqing Gao, Zhiming Huang, "Improvements in electrical properties, low frequency noise and detection performance of a Mn-based bilayer thin film infrared detector", *Sensors and Actuators A* 283, 196–203 (2018).
- [52] M. C. Foote, M. Kenyon, T. R. Krueger, T.A. McCann, R. Chacon, E.W. Jones, M.R. Dickie, J.T. Schofield and D.J. McCleese, "Thermopile detector arrays for space science applications", *International Thermal Detectors Workshop (TDW 2003)*, p. 2-16 – 2-20 (2003). NASA/CP-2004-212748 <https://ntrs.nasa.gov/search.jsp?R=20040068195>
- [53] Frank Haenschke, Ernst Kessler, Ulrich Dillner, Andreas Ihring, Uwe Schinkel, and Hans-Georg Meyer, "New high detectivity linear array for analytical measurement in the room temperature range", *Proceedings of Infrared Technology and Applications XXXVIII, Proc SPIE 8353*, 83531L (2012).
- [54] Anand S. Gawarikar, Ryan P. Shea, and Joseph J. Talghader, "High Detectivity Uncooled Thermal Detectors With Resonant Cavity Coupled Absorption in the Long-Wave Infrared", *IEEE Trans. Elec. Dev.* 60 (8), 2586–2591 (2013).
- [55] Cheng Lei, Haiyang Mao, Yudong Yang, Wen Ou, Chenyang Xue, Zong Yao, Anjie Ming, Weibing Wang, Ling Wang, Jiandong Hu, Jijun Xiong, "A double-end-beam based infrared device fabricated using CMOS-MEMS process", *Sensor Review* 36 (3), 240–248 (2016).
- [56] Wenjian Ke, Yi Wang, Hong Zhou, Tie Li and Yuelin Wang, "Design, fabrication, and characterization of a high-performance CMOS-compatible thermopile infrared detector with self-test function", *J. Micromech. Microeng.* 28, 125017 (2018).
- [57] Ting-Wei Shen, Kai-Chieh Chang, Chih-Ming Sun and Weileun Fang, "Performance enhance of CMOS-MEMS thermoelectric infrared sensor by using sensing material and structure design", *J. Micromech. Microeng.* 29, 025007 (2019).
- [58] Wei Li, Zao Ni, Jiachou Wang, and Xinxin Li, "A Front-Side Microfabricated Tiny-Size Thermopile Infrared Detector With High Sensitivity and Fast Response", *IEEE Trans. Elec. Dev.* 66 (5), 2230–2237 (2019).
- [59] Paul W. Kruse, "A Comparison of the limits to the performance of thermal and photon detectors imaging arrays", *Infrared Phys. Technol.* 36, 869-882 (1995).
- [60] M. Rull-Bravo, A. Moure, J. F. Fernández, and M. Martín-González, "Skutterudites as thermoelectric materials: revisited", *RSC Advances* 5, 41653 (2015).

[61] Xinqi Chen, Wei Dai, Tian Wu, Wei Luo, Jianping Yang, Wan Jiang, and Lianjun Wang, "Thin Film Thermoelectric Materials: Classification, Characterization, and Potential for Wearable Applications", *Coatings* 8, 244 (2018).

[62] Bhuvanesh Srinivasan, Alain Gellé, Francesco Gucci, Catherine Boussard-Pledel, Bruno Fontaine, Régis Gautier, Jean-François Halet, Michael J. Reece, and Bruno Bureau, "Realizing a stable high thermoelectric $zT \sim 2$ over a broad temperature range in $\text{Ge}_{1-x-y}\text{Ga}_x\text{Sb}_y\text{Te}$ *via* band engineering and hybrid flash-SPS processing", *Inorganic Chemistry Frontiers* 6, 63–73 (2019).

[63] Rama Venkatasubramanian, Edward Siivola, Thomas Colpitts, and Brooks O'Quinn, "Thin-film thermoelectric devices with high room-temperature figures of merit", *Nature* 413, 597–602 (2001).